Steering S-scheme charge transfer via interfacial dipole induced by amine-containing polyelectrolyte

Tao Li [1], Chuang Feng [1], Biquan Xiong [2], Xuhui Zhu [1], Zhicai He [1*] & Wai-Yeung Wong [2*]

[1] *Institute of Polymer Optoelectronic Materials and Devices, State Key Laboratory of Luminescent Materials and Devices, School of Material Science and Engineering, South China University of Technology, Guangzhou 510640, P. R. China*

[2] *Department of Applied Biology & Chemical Technology and Research Institute for Smart Energy, The Hong Kong Polytechnic University, Hung Hom, Hong Kong, P. R. China*

The lack of a robust interfacial driving source over multicomponent photocatalysts is an essential contributor to the sluggish spatial charge transfer across the heterointerface and severe carrier recombination, thereby rendering maneuvering charge transfer of composite materials a thorny issue. Herein, we demonstrate an electric dipole moment-driven charge transfer photosystem utilizing amine-containing polyfluorene polyelectrolyte (i.e., PFN) and inorganic semiconductor matrices (i.e., WO_3) as the building blocks to direct the interfacial charge transfer, effectively targeting the photoexcited charge carriers to the active sites. Experimental results and theoretical simulations reveal that the electronic coupling interaction between the pendant electron-rich amine groups along the PFN backbone and WO_3 surface enables the nonuniform charge distribution at the interface over WO_3@PFN heterojunction, which ultimately fosters the formation of interfacial dipole oriented from conjugated macromolecular backbone of PFN to the surface of WO_3 matrices. The interfacial dipole with excellent charge transfer kinetics spontaneously activates the unidirectional and accelerated S-scheme charge motion from the WO_3 framework to the conjugated chain of PFN due to the suitable band offsets at the interface, thus endowing WO_3@PFN heterostructures with a significantly enhanced net efficiency of photoactivity. These findings would provide some insights into the design of advanced heterojunction photocatalysts for solar energy conversion as well as the study of the working mechanism of polyelectrolyte interlayers in optoelectronic devices.

photocatalysis, heterojunction, interfacial dipole, polyelectrolyte, s-scheme

Citation: Li T, Feng C, Xiong BQ, Zhu XH, He ZC, Wong WY. Steering s-scheme charge transfer via interfacial dipole induced by amine-containing polyelectrolyte. *Sci China Chem*, 20**, **: 1−2, doi: ********

1 Introduction

Efficient solar energy utilization could alleviate many energies and environmental issues, as the solar energy irradiating the surface of the earth exceeds the current global human energy consumption by roughly four orders of magnitude.[1-3] As one of the most promising techniques to efficiently utilize solar energy, semiconductor-mediated photocatalysis has been drawing increasing attention and significant achievements have been made to date.[4-6] Despite considerable efforts, inefficient charge separation and transportation remain to be the most challenging factors restricting any practical applications of photocatalysis. Generally speaking, there is a lack of intrinsic driving force over photocatalysts to direct charge separation and transportation.[7] As a result, only a tiny fraction of the photo-generated electrons and holes can be separated successfully, and the majority are consumed through recombination. The construction of heterojunctions using composite materials with different energy band structures can

*Corresponding authors (email: zhicaihe@scut.edu.cn; wai-yeung.wong@polyu.edu.hk)

facilitate carrier separation and migration at the interface.[8-10] The introduction of an internal electric field (IEF) in the heterojunction can serve as an intrinsic driver to control the migration path of photogenerated carriers, thereby more effectively increasing the lifetime of photogenerated carriers.[11, 12] Among the plethora of heterojunctions photocatalysts with diverse charge-transfer routes, step-scheme (S-scheme) heterojunctions have received tremendous attention on account of unique structural advantages in comparison with conventional heterojunctions including efficient spatial charge separation, longer carrier lifetimes, and excellent reduction and oxidation abilities.[13-16] The S-scheme photocatalytic principle was first proposed by Yu et al.,[17] and they prepared 2D WO_3/g-C_3N_4 S-scheme heterojunctions with excellent charge separation and transfer for photocatalytic H_2O splitting into H_2. In recent years, S-scheme heterojunctions have witnessed their widespread exploration in a myriad of fields such as photocatalytic water splitting,[18-20] photocatalytic CO_2 reduction,[16, 21, 22] and organic photosynthesis.[23-25] In short, the construction of S-scheme heterojunctions is an ideal strategy to preserve effective carriers and suppress their recombination.

π-conjugated polyelectrolytes (CPEs) have been extensively investigated for photocatalytic and organic photo-electronic applications by virtue of their enormous structural diversity and tunability in terms of potential properties or processability.[26-28] Notably, CPEs differ from ordinary conductive polymers with a conjugated structure in that they have different polar functional groups grafted on the molecular backbone, which makes them exhibit excellent performance as an interlayer in various photoelectric conversion devices.[29, 30] The polar functional groups with electron-donating or electron-withdrawing characteristics could result in the electronic coupling interaction between the CPEs and neighboring material via intermolecular charge transfer, ultimately leading to the formation of space charge region (i.e., interfacial dipole).[31, 32] The interfacial dipole generated in the CPEs interlayers is proposed to enhance the built-in potential of organic photovoltaics through the superposition effect of the electric field, thereby boosting the device performance in all aspects.[33-35] It can thus be envisioned that, if one could somehow graft the CPEs containing polar functional groups onto another material, in this scenario, these polar functional groups can produce a unidirectional interfacial dipole between the conjugated macromolecular backbone of CPEs and the neighboring material, which can serve as a direct driving force to stimulate instant charge migration between the assembly units. In addition, the interface of the CPEs-involved heterojunction photosystem can be flexibly and readily realized by molecular interactions via solution-processing methods like self-assembling.

With these considerations, an interfacial dipole-driven charge modulation system was designed by electrostatically assembling the polar amine-containing polyfluorene PFN (poly[(9,9-dioctyl-2,7-fluorene)-alt-(9,9-bis(3'-(N,N-dimethylamino)propyl)-2,7-fluorene)]) onto one-dimensional WO_3 nanorods (NRs), and the resulting configuration (i.e., WO_3@PFN) featured a well-defined core-shell heterojunction structure. We found that the polar amino groups grafted onto the molecular backbone of PFN redistributed the charges between the WO_3 core and PFN shell and fostered a microscopic electric dipole moment with the positive charge end pointing toward the conjugated macromolecular backbone of PFN and the negative charge end pointing toward the surface of WO_3. This is shown by theoretical simulations and experimental results. More intriguingly, owing to the presence of interfacial dipole, the WO_3@PFN core-shell heterojunction can be represented in an S-scheme charge flow model, leading to effectively the slowing-down of the electron-hole recombination and prolonged lifetime of the charge carriers. This ultimately results in remarkably improved photoactivity.

2 Results and discussion

The flowchart for constructing WO_3@PFN core-shell heterojunctions is illustrated in **Figure 1a**. Initially, the WO_3 NRs were prepared by a modified hydrothermal method.[36] Field-emission scanning electron microscopy (FESEM) images display that as-prepared WO_3 NRs were composed of uniformly oriented microrods having lengths of several micrometers (**Figure S1**). From the FESEM images, most NRs can be seen to aggregate into organized bundles. The oriented anchoring of PFN species onto the WO_3 surface was achieved by the electrostatic linkage between negatively charged WO_3 and positively charged PFN stems from the partial protonation of the amine group, based on the zeta potential analysis in **Figure 1b**. In this regard, attracted by the substantial electrostatic forces, PFN can be spontaneously and uniformly wrapped on the WO_3 framework, resulting in a well-defined WO_3@PFN core-shell heterostructure. By adjusting the concentration of PFN solution (0.5, 1.0, and 2.0 mg mL^{-1}), a series of core-shell heterojunctions of WO_3@PFN with different anchoring amounts of PFN were obtained, respectively labeled as WO_3@PFN0.5, WO_3@PFN1.0, and WO_3@PFN2.0. The mass ratio of PFN to WO_3 over composite heterojunctions was accessed by thermogravimetric (TG) analyses (**Figure S2**). As can be seen, all WO_3@PFN heterojunctions exhibit a two-step thermal degradation process with about 1.4%, 1.5%, and 2.0% mass loss up to around 600 °C, respectively, which originates from the pyrolysis of the conjugated macromolecular backbone of the PFN covered layer. Subsequently, Fourier transform infrared (FTIR) analysis was carried out to collect the structural information of the samples (taking WO_3@PFN1.0 as an example, since it shows the best photoactivity according to the later activity test, and unless it is specified further, the following characterizations will also mainly focus on WO_3@PFN1.0). As presented in

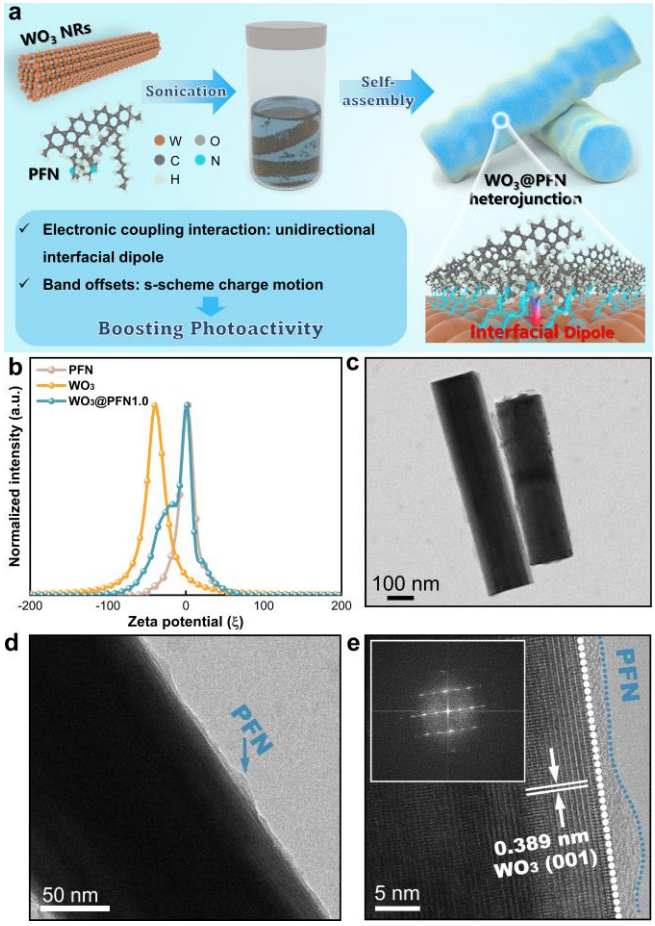

Figure 1 (a) The schematic illustration of the synthetic process. (b) Zeta potentials of PFN, WO_3 , and WO_3@PFN. (c, d) TEM images and (e) HRTEM image of WO_3@PFN1.0.

Figure S3 and **Table S1**, the bands of WO_3@PFN1.0 located at 3595, 3535, and 3460 cm^{-1} could be ascribed to the stretching vibration of surface hydroxyl (–OH), while those at 1621 and 1599 cm^{-1} corresponds to bending vibration of W–OH and W–O bonds, respectively.[37, 38] Meanwhile, several enriched characteristic vibration modes, belonging to the encapsulated PFN layer, e.g., the stretching vibrations of $–CH_2$ groups (the peaks within the range of 2956–2848 cm^{-1}) and bending mode of C–N (1461 cm^{-1}) groups,[39, 40] were also recorded in the FTIR spectrum of WO_3@PFN1.0. Transmission electron microscopy (TEM) images of WO_3@PFN1.0 in **Figure 1c**, **d** confirm the rod-like morphology of the WO_3 matrix, onto which a rough layer of amorphous PFN is adhered in a thin manner on the border of WO_3, giving direct evidence for the well-defined core-shell heterojunction by the in situ electrostatic self-assembly method. High-resolution TEM (HRTEM) images reveal phase junctions between the shell and core regions at the contact interface. As displayed in **Figure 1e**, the distinct lattice fringe with *d*-spacings of 0.389 nm matches with the (001) crystal facets of hexagonal WO_3 core (JCPDS No. 75–2187) according to the X-ray diffraction (XRD) patterns (**Figure S4**);[41] PFN shell is ultrathin (ca. 2 nm) to be transparent and closely tethered on the whole WO_3 core framework.

Previous theoretical studies demonstrate that surface states have a substantial impact on the electronic structure of catalyst hosts,[42, 43] e.g., incorporation of electron-donating moieties into the catalyst surface could trigger electron accumulated surface by intermolecular charge transfer. In our case, the PFN shell tightly attaches to the WO_3 framework by the electrostatic forces between the electron-rich amine group and WO_3 surface; those amine groups bearing electron-donating capability may conduct the charge transfer interaction with neighboring WO_3, favoring the formation of the interfacial electrical dipole between WO_3 and the conjugated backbone of PFN. To substantiate this speculation, scanning Kelvin probe (SKP) measurement was conducted to probe the variation in local work function (WF) of the WO_3 surface before and after PFN coating. Generally, the change in WF can be reflected by the contrast contact potential difference (CPD) between the sample surface and the standard gold tip as a reference.[44] As shown in **Figure 2a**, the surface potential is uniform over PFN, WO_3, and WO_3@PFN1.0, but there is a very significant difference in CPD values between them. The PFN features a much higher surface potential (309 mV), while the surface potential of WO_3 is very low (-315 mV). After encapsulation with PFN, the surface potential of the WO_3@PFN1.0 heterojunction sharply increases to -89 mV, implying the existence of electronic coupling interaction between PFN and WO_3. The WF can be estimated from the CPD results by the function:

$$WF = WF_{tip} - e \times CPD$$

where WF_{tip} is the work function of the standard gold tip (4.25 eV) and e denotes the electron charge. Based on this, the WF values of PFN, WO_3, and WO_3@PFN1.0 were determined to be 3.94, 4.56, and 4.34 eV, respectively. The WF value of WO_3@PFN1.0 is between WO_3 and PFN, substantiating the presence of the electron-transfer interaction from the PFN shell to the WO_3 core. This result proves that PFN functions as a charge donor and provides electrons to neighboring WO_3, building the electron depleted PFN surface and electron accumulated WO_3 surface in the heterointerface. Therefore, a microscopic electric dipole moment with the positive charge end pointing toward the conjugated macromolecular backbone of PFN and the negative charge end pointing toward the surface of WO_3 can be established (**Figure S5**). The interfacial dipole intensity was measured based on the model proposed by Kanata et al. (The information on the model is provided in the Supporting Information).[45-47] According to the model, the interfacial dipole intensity is determined by the surface voltage (V_s) and the surface charge density (ρ). Compared to WO_3, WO_3@PFN heterojunctions gradually yield enhanced surface photovoltage response (**Figure S6**) and photocurrent density (**Figure S7**) with increasing the encapsulation concentration of PFN precursor from 0.5 to 2.0 mg mL^{-1}. Consequently, as displayed in

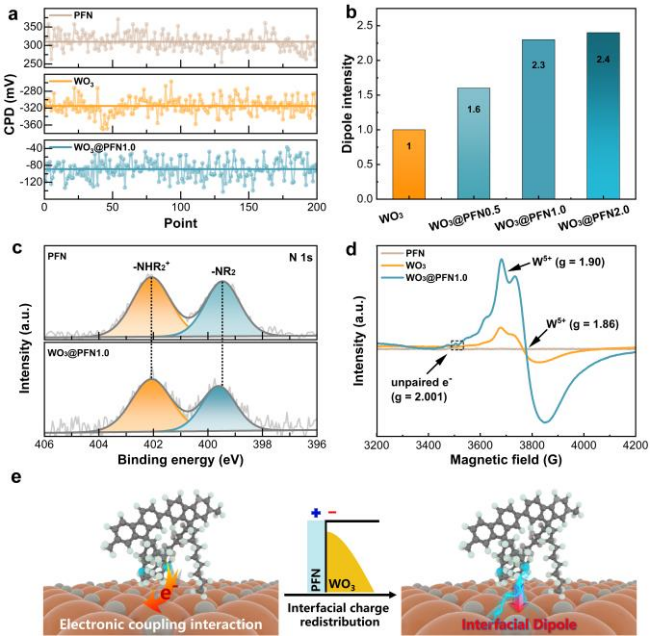

Figure 2 (a) SKP measurement results of PFN, WO_3 and WO_3@PFN1.0. (b) Interfacial dipoles intensity (assuming the intensity of WO_3 to be 1) for WO_3@PFN. (c) High-resolution N 1s spectra of pure PFN and WO_3@PFN1.0. (d) EPR spectra of PFN, WO_3, and WO_3@PFN1.0. (e) Illustration of the formation mechanisms of interface dipole of WO_3@PFN1.0 heterojunction.

Figure 2b, the dipole intensity of optimal WO_3@PFN heterojunctions is greatly advanced to more than twice that of pristine WO_3.

As elucidated above, we reason that the interaction of the electron-rich polar amine group at the side chain of PFN with the WO_3 surface plays a crucial role in forming the interfacial dipole. Herein, X-ray photoelectron spectroscopic (XPS) analysis was used to validate the interaction of the PFN shell and WO_3 core. The survey XPS spectrum of WO_3@PFN1.0 heterojunction demonstrates the W 4f, O 1s, and C 1s core elements (**Figure S8**). **Figure 2c** shows the high-resolution N 1s XPS spectra of pure PFN and WO_3@PFN1.0 heterojunction, in which the peaks at around 402.1 and 399.5 eV for pure PFN are assigned to the charged ammonium group ($–NHR_2^+$) and amine group ($–NR_2$), respectively.[48] Compared with PFN, the $–NR_2$ peak position for WO_3@PFN1.0 exhibits a shift of 0.2 eV toward higher binding energy, and simultaneously, a downshift in the binding energy is observed in the high-resolution W 4f and O 1s spectra of the WO_3@PFN1.0 with respect to those of the pristine WO_3 (**Figure S9** and **Table S2**). No perceivable binding energy shift in $–NHR_2^+$ peak. The increase in binding energy indicates the weakened electron screening effect due to the decrease of the electron concentration, whereas the decrease of binding energy means an increase in electron concentration.[49] This implies a charge transfer has occurred from the PFN shell to the WO_3 core via the strong electron-donating $–NR_2$ groups. The suggested charge distribution at the interface is shown in **Figure 2e**. Further evidence of the interfacial dipole moment is shown in the electron paramagnetic resonance (EPR) analysis (**Figure 2d**) and Raman spectra (**Figure S10**). As showcased in **Figure 2d**, WO_3 features distinctive EPR signals of paramagnetic W^{5+} (g = 1.90 and 1.86) generated due to oxygen vacancies.[50, 51] Compared to single-component WO_3, the EPR signals of spin active W^{5+} sites over WO_3@PFN1.0 heterojunctions are significantly enhanced and a characteristic signal of unpaired electron at g = 2.001 is detected for the WO_3@PFN1.0 heterojunction. The signal of unpaired electron in PFN spectra is almost negligible. This increase of W^{5+} species in the WO_3@PFN1.0 heterojunctions has also been supported by a larger area-ratio of the W^{5+} peak in W 4f XPS spectra. Considering that there is no significant increase in the area ratio of oxygen vacancies between WO_3 and WO_3@PFN1.0 heterojunctions, the higher number of spin active W^{5+} and unpaired electrons in WO_3@PFN1.0 heterojunctions most likely originates from the borrowing of an electron from the pendant amine lone pair orbitals of PFN to W^{6+} species of WO_3. This result further substantiates the presence of the synergistic interaction at the interface between the building blocks, engendering the interface dipole.

Density function theory (DFT) calculations were performed to render some general insights into the molecular binding geometry and interfacial interaction mechanisms of the PFN on WO_3. The most stable structure of the PFN monomer molecule on the surface of WO_3 matrices is shown in **Figure S11**. The proof of the interfacial dipole is obtained by calculation of the charge density difference (Δρ) by subtracting the electronic charge of PFN monomer and WO_3 (001)

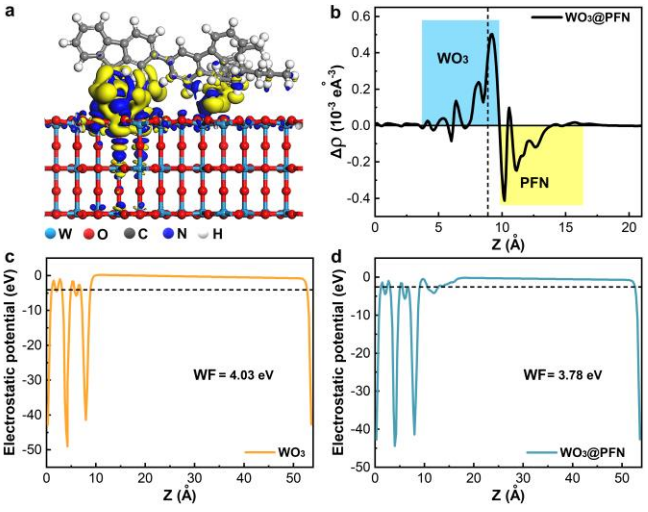

Figure 3 (a) The isosurface of charge density difference for PFN on the surface of WO_3 (001), the blue and yellow represent the increase and decrease distributions of electron density, respectively. (b) Electron density difference along the surface normal (z) averaged over the xy plane in unites of $Å^{-3}$ of PFN on the surface of WO_3 (001). Calculated electrostatic potentials for (c) WO_3 and (d) WO_3@PFN.

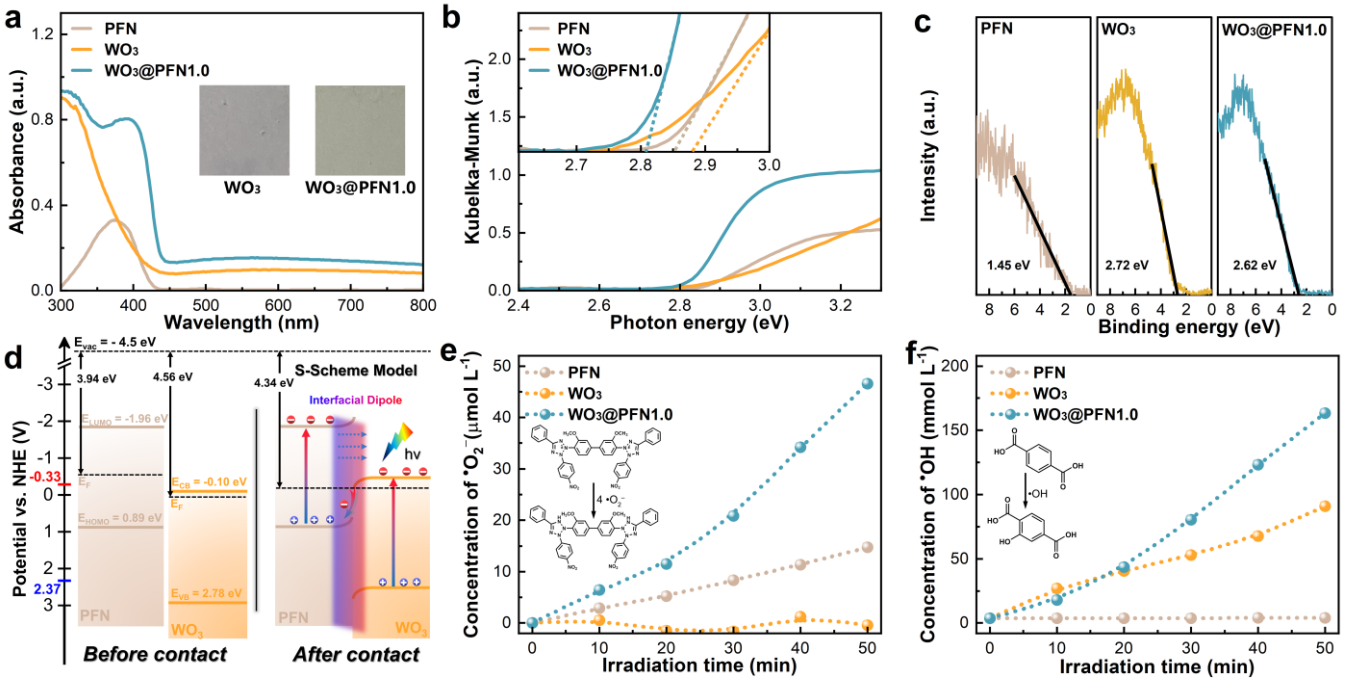

Figure 4 (a) DRS spectra, (b) Tauc plots, and (c) VB-XPS spectra of PFN, WO_3, and WO_3@PFN1.0. (d) Energy band configuration and photoinduced charge-carriers transfer process over WO_3@PFN. (e) $^{\bullet}O_2^-$ and (f) $^{\bullet}OH$ radicals evolution over PFN, WO_3, and WO_3@PFN1.0.

from that of WO_3@PFN heterojunction. As shown in **Figure 3a**, both the charge accumulation (blue) and depletion (yellow) located at the interface indicate the presence of strong interaction at the interface, wherein the charge accumulation occurs near the edge of WO_3 matrices, while the charge depletion occurs around the amine group of PFN monomer at the interface. The result validates that there is an obvious electron transfer from the amine group at the side chain of PFN ($\Delta\rho < 0$) to the surface of WO_3 matrices ($\Delta\rho > 0$) in the ground electronic state, leading to the interfacial charge redistribution (**Figure 3b**). Additionally, the WF of WO_3 and WO_3@PFN heterojunctions were calculated. As displayed in **Figure 3c**, **d**, after the PFN monomer is introduced into the WO_3 (001) model, the WF value of WO_3@PFN heterojunction decreases, which is consistent with CPD results, once again substantiating the presence of the electron-transfer interaction from PFN to the WO_3. Accordingly, an interface dipole moment would be established at the interface with the direction from the conjugated backbone of PFN to the surface of WO_3 matrices. These results, in combination with the above characterization (i.e., SKP, XPS, and EPR) results, provide solid evidence for the formation of a robust interfacial dipole field.

The existence of the interfacial dipole would facilitate the photogenerated carrier separation and migration across the heterointerface over the WO_3@PFN heterojunction. Therefore, the precise band location of each building block of the heterojunctions was initially evaluated to unlock the space charge transfer pathway between them. The bandgap (E_g) of PFN and WO_3 are obtained by transforming the UV–vis diffuse reflectance spectra (DRS) to the Tauc plot as depicted in **Figures 4a**, **b**, and **Figure S12**. There are two absorption bands in the DRS result of WO_3@PFN, one with the edge at around 420 nm ascribed to band-gap absorption of the WO_3 core, and one with the edge extended to 440 nm assigned to the PFN shell. According to the Tauc plot, the E_g values of PFN and WO_3 are determined to be 2.85 and 2.88 eV, respectively. The valence band potentials (E_{VB}) and highest occupied molecular orbital potentials (E_{HOMO}) were determined with VB-XPS measurements. **Figure 4c** shows the magnified VB-XPS spectra for PFN, WO_3, and WO_3@PFN1.0 samples. The E_{VB} value relative to normal hydrogen electrode (vs NHE) can be calculated according to the formula:

$$E_{VB} = WF + E - 4.5$$

where WF is the work function obtained by the CPD results and E is the extrapolation value in the valence band region. Therefore, the E_{VB} (or E_{HOMO}) values of PFN, WO_3, and WO_3@PFN1.0 are 0.89, 2.78, and 2.46 eV, respectively. It is noteworthy that an upshift in the WF and E_{VB} of WO_3@PFN1.0 heterojunction is observed relative to WO_3, suggesting the band bending in energy band configurations of the assembly units. Based on our experimental studies and theoretical simulations, when PFN is directionally deposited on the WO_3 substrate enabled by self-assembly, there is an interfacial dipole pointing from the PFN shell to the WO_3 core across the heterointerface in WO_3@PFN heterojunction stemming from the interfacial charge redistribution, which would lead to positive energy band bending of PFN component and negative energy band bending of WO_3

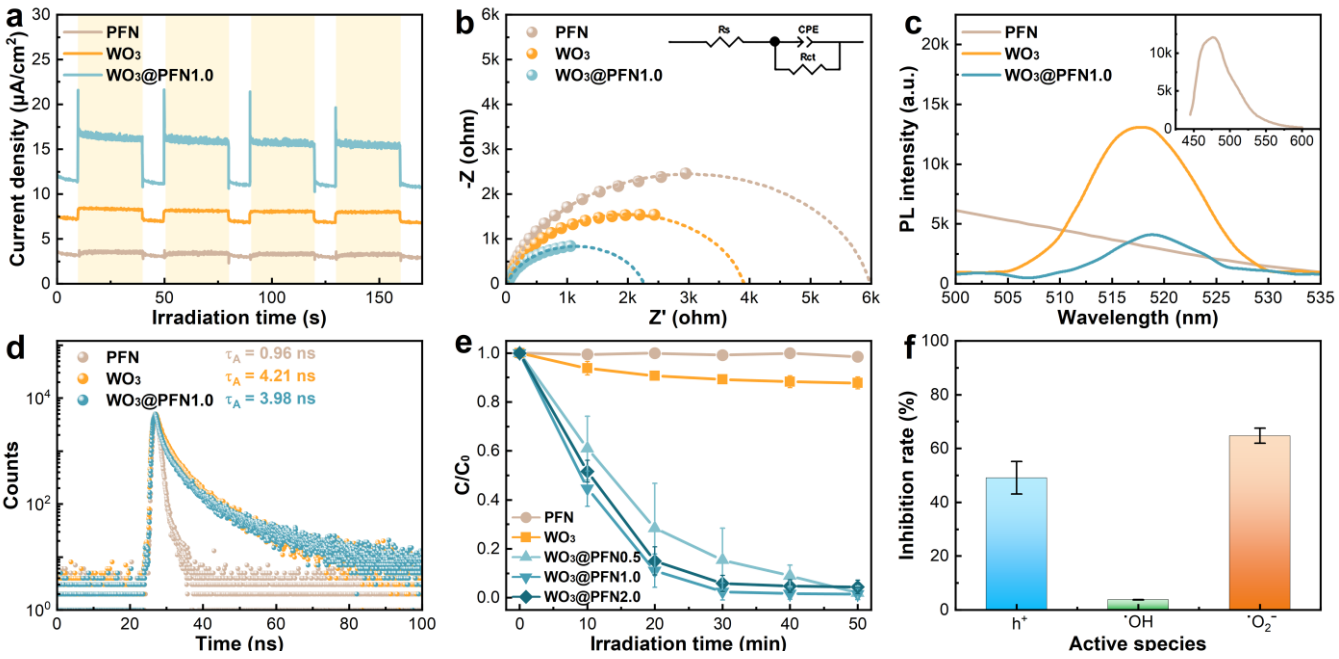

Figure 5 (a) *I–t* spectra (bias: 1.23 V vs RHE; light source: 100 mW cm^{-2}, AM 1.5G), (b) EIS Nyquist plots (bias: 0.6 V vs RHE), (c) PL emission spectra, and (d) TRPL spectra of PFN, WO_3, and WO_3@PFN1.0. (e) Time-dependent photocatalytic mineralization of RhB of the as-synthesized samples under full-spectrum light irradiation. (f) The contribution of various active species to RhB mineralization in free radical quenching experiments.

component. In this scenario, upon the inter-band excitations of PFN and WO_3 component, the photoinduced electrons on the conduction band of WO_3 may spatially migrate to the valence band of PFN for quenching the photoinduced holes through an S-scheme of charge transfer process across the heterointerface. By combining the above results, the relative band structure alignment of the heterojunction with the speculative charge transfer model is illustrated in **Figure 4d**.

The detection of molecular oxygen active species is an effective way to validate the photogenerated charge transfer pathways.[21, 52] The nitroblue tetrazolium (NBT) can react with superoxide radicals ($^{\bullet}O_2^-$) and displays a maximum absorbance at 259 nm (**Figure S13**), thus can be used to ascertain the generated amount of $^{\bullet}O_2^-$ over catalysts by recording the reduction of NBT on the spectrophotometer. Based on the reacting relation between NBT and $^{\bullet}O_2^-$ (1:4 in molar ratio), the $^{\bullet}O_2^-$ evolution curves of PFN, WO_3, and WO_3@PFN1.0 are displayed in **Figure 4e**. Rapid $^{\bullet}O_2^-$ evolution has occurred over PFN and WO_3@PFN1.0; the $^{\bullet}O_2^-$ evolution rate over WO_3@PFN1.0 is much high than that of pure PFN. While no perceivable signal of $^{\bullet}O_2^-$ can be detected in WO_3 due to the inferior E_C (0.04 V vs. NHE) in contrast with the reaction energy potential of $O_2/^{\bullet}O_2^-$ (-0.33 V vs. NHE). Additionally, terephthalic acid (TA) is used as a probing agent for detecting $^{\bullet}OH$ radicals. Due to their reaction production having a specific fluorescence emission with a maximum intensity at 425 nm, the amount of $^{\bullet}OH$ radicals can be determined by exciting the sample at 315 nm and measuring the intensity at 425 nm (**Figure S14**). The WO_3@PFN1.0 displayed a substantially greater TA–$^{\bullet}OH$ evolution in **Figure 4f** by comparing to the signals of pure WO_3; as expected, the TA–$^{\bullet}OH$ evolution over PFN is negligible due to the larger oxidation potential of $H_2O/^{\bullet}OH$ (2.37 V vs. NHE). The above results have undoubtedly confirmed the generation of $^{\bullet}O_2^-$ and $^{\bullet}OH$ radicals over WO_3@PFN1.0 heterojunction, which indicates that the S-scheme heterojunction is more likely to occur than conventional heterojunctions under this circumstance. Additionally, higher concentrations of $^{\bullet}O_2^-$ and $^{\bullet}OH$ radicals mean more electrons and holes are accumulated on the conduction band of PFN and valence band of WO_3 through an exceptional S-scheme charge transfer process derived by an interfacial dipole, respectively.

To further understand the significance of the spatial S-scheme charge separation pattern induced by the interfacial dipole driving force, we first detected the interfacial charge separation efficiency by photoelectrochemical (PEC) measurements under full-spectrum light. The photoanodes were prepared by dropwise the sample inks on the pretreated FTO and then dried for 24 h at ambient temperature (**Figure S15**). **Figure 5a** portrays the on-off transient photocurrent response (*I–t*) of different photoanodes, wherein WO_3@PFN1.0 yields an enhanced photocurrent intensity compared to others when the light is on. The ameliorative photocurrent implies a more effective charge separation efficiency over WO_3@PFN1.0 than PFN and WO_3. Notably, the direct dropping of PFN on the WO_3 photoanodes could not readily boost the photocurrent intensity of WO_3 photoanodes (**Figure S16**), meaning that the well-defined interface interaction of the WO_3 matrix and ultrathin PFN

shell is required for the considerably increased charge separation efficiency of WO_3@PFN1.0 heterojunction. Moreover, as observed from the electrochemical impedance spectroscopy (EIS) Nyquist plots in **Figure 5b**, all the samples exhibit similar semicircles, and WO_3@PFN1.0 features the smallest arc size. The solid interface delamination resistance and the surface charge transfer resistance could be reflected by the radius of the arc in the EIS spectra, and the smaller radius of the arc indicated a more effective separation of photogenerated carriers.[53, 54] The fitted EIS results of photoanodes based on an equivalent circuit (inset in **Figure 5b**) are summarized in **Table S3**. Charge transfer resistances of PFN, WO_3, and WO_3@PFN1.0 are determined as 7540, 5022, and 2987 Ω cm^2, respectively. Moreover, as shown in the EIS Bode plots (**Figure S17**), WO_3@PFN1.0 features a significant blue shift in the low-frequency peak; meanwhile, the phase angle in the low-frequency region for WO_3@PFN1.0 is much smaller. The low-frequency peak corresponds to the slow catalytic reactions at the electrode/electrolyte interface,[55, 56] and this result indicates that the encapsulation of WO_3 with the PFN layer promotes catalytic reaction kinetics at the electrode, stemming from the efficient charge transfer between them.

Furthermore, the S-scheme charge transfer dynamics were investigated in depth by steady-state photoluminescence (PL) and time-resolved photoluminescence (TRPL) studies. As shown in **Figure 5c**, WO_3@PFN1.0 exhibited the PL peak of WO_3 centered at 518 nm. However, its PL emission intensity is significantly quenched compared to that of pure WO_3. TRPL spectra were conducted to understand the carrier dynamics quantitatively. **Figure 5d** manifests an accelerated PL decay for WO_3@PFN1.0 heterojunction with respect to unitary WO_3. Notably, PFN yields the fastest decay rate, which is related to the intrinsic properties of organic semiconductors that the excitons generated by photoexcitation cannot be dissociated at room temperature.[57] After fitting the decay curves with a model of two exponential functions (**Table S4**), the average PL lifetimes (τ_{av}) of PFN, WO_3, and WO_3@PFN1.0 were calculated to be 0.96, 4.21, and 3.98 ns, respectively. The quenched PL intensity and accelerated PL decay indicated the effective charge transfer between WO_3 and PFN. More importantly, the contribution of the short decay component (A_1) of the TRPL profiles underwent an increase from 68.5% to 76.2% as the WO_3 was merged with PFN, revealing that the electron transfer from the WO_3 core to the PFN shell is involved at the interface of WO_3@PFN1.0 core-shell heterojunction. Taken together, it is beyond doubt that the photogenerated carrier separation efficiency of WO_3@PFN1.0 is greatly advanced through an exceptional photogenerated carrier separation model derived by the robust interfacial dipole that stems from electronic coupling interaction between the amine-containing PFN shell and WO_3 core. Consequently, enhanced photocatalytic activity in WO_3@PFN heterojunction can be expected.

The composite samples were utilized for the photocatalytic mineralization of RhB under full-spectrum light irradiation as a function of irradiation time and compared with unitary PFN and WO_3. Blank experiments in the absence of a catalyst or light (**Figure S18**) corroborate that the reaction is a photocatalytic process. As displayed in **Figure 5e** and **Figure S19**, all WO_3@PFN heterojunctions exhibit remarkably enhanced photocatalytic performances with excellent reaction rates in comparison to the single component under the same experimental conditions. Regarding the fact that PFN has almost no photoactivity and pure WO_3 demonstrates inferior mineralization efficiency of RhB, the enhanced photocatalytic activity of WO_3@PFN heterojunctions could be attributed to the formed high-quality interfaces facilitating the diffusion and transportation of charge carriers. Noteworthily, the photoactivities of all WO_3@PFN heterojunctions derived from standard deviations of degradation curves are similar, which means their efficient charge separation efficiency induced by the interfacial dipole. In order to accurately assess the effect of PFN content on photocatalytic performance, a set of experiments was conducted (**Figure S20**, see the discussion in the Supplementary Information). The photostability of the PFN shell in heterojunction during the long-time photocatalytic reaction has been evaluated. As shown in **Figure S21**, the peak intensity and position of typical functional groups of PFN show slight changes after the cyclic reaction, as revealed by the FTIR spectra, which can be attributed to the gradual dissolution of water-soluble PFN or an alternate in the surface chemical environment caused by adsorption of trace amounts of the reaction solution. This phenomenon was also confirmed by N 1s XPS spectra. Nonetheless, no obvious new peaks were found in the XPS spectra, verifying the relatively favorable photostability of the PFN shell.

The free radical quenching experiments were performed by adding triethanolamine (TEOA), tert-butanol (TBA), and benzoquinone (BQ) to the reaction system to quench h^+, $^{\bullet}OH$, and $^{\bullet}O_2^-$, respectively. As displayed in **Figure S22**, the inhibited photocatalytic activity of WO_3@PFN1.0 was observed when these three scavengers were added to the reaction system, among which the photoactivities of WO_3@PFN1.0 decreased dramatically with the addition of TEOA and BQ, while TBA caused only a slight reduced photoactivity, implying that h^+ and $^{\bullet}O_2^-$ radicals contribute mainly to the photoactivity enhancement (**Figure 5f**). Moreover, high resolution mass spectrum (HRMS) was conducted to determine the degradation pathways of RhB over WO_3@PFN1.0. As shown in **Figure 6a**, before the photodegradation, the peak of m/z = 443.23 corresponding to the RhB matrix was detected. With increasing reaction time, additional peaks of m/z = 415.20, 387.17, 359.14, 331.11 could be observed, which can be assigned to the following N-deethylated degradation intermediates: N,N-diethyl-N'-ethylrhodamine (DER), N-ethyl-N'-ethylrhodamine (EER), N-ethylrhodamine (ER), and rhodamine (R). After the photodegradation for 30 min, the N-deethylated intermediates could

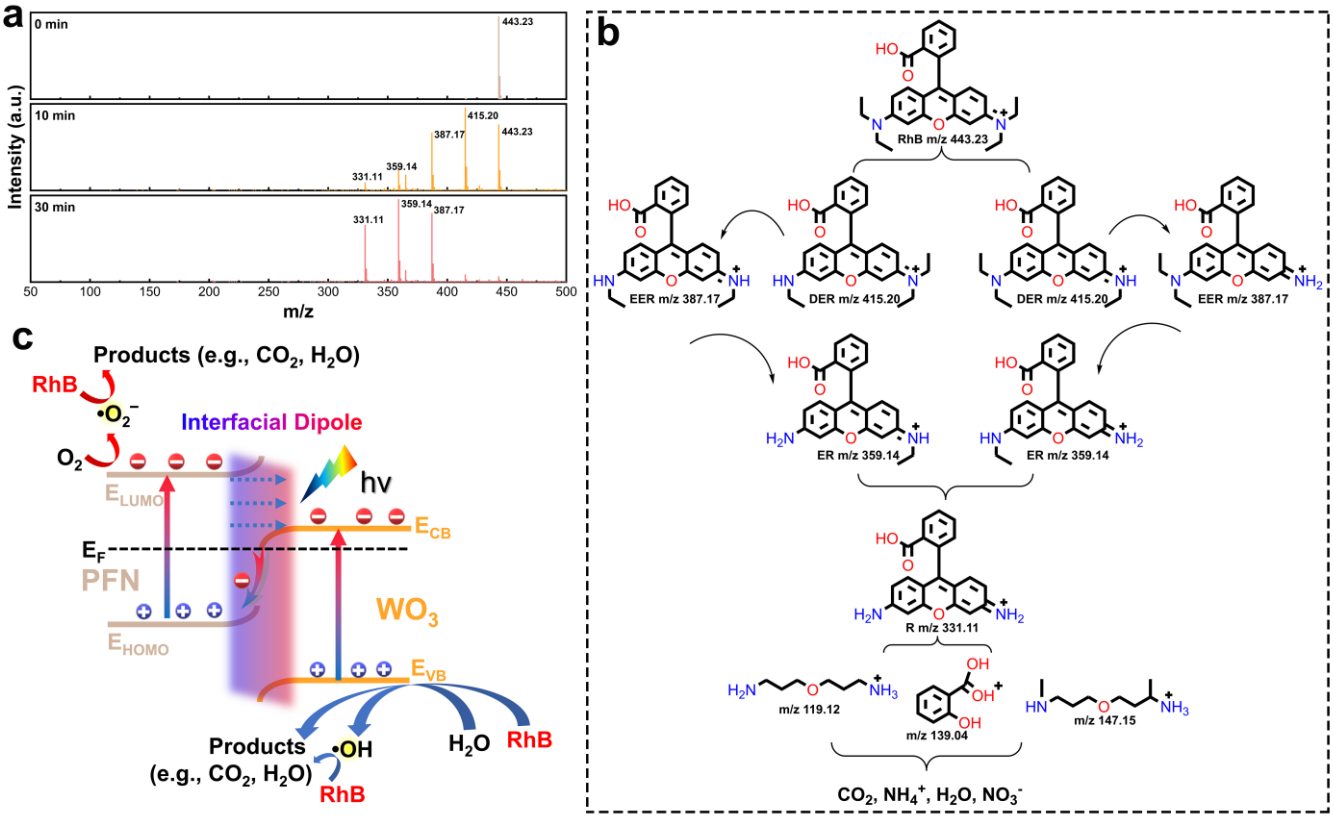

Figure 6 (a) HRMS of degradation products toward RhB under different irradiation times over WO_3@PFN1.0. (b) Photodegradation pathway of RhB. (c) Schematic illustration depicting the photocatalysis mechanism of WO_3@PFN heterojunction.

further degrade into small organic molecules and eventually mineralized into CO_2, NH_4^+, H_2O, and NO_3^-. According to the HRMS results, the possible photodegradation pathway of RhB over WO_3@PFN1.0 is proposed in **Figure 6b**. Considering that the generation of $^{\bullet}O_2^-$ and $^{\bullet}OH$ radicals has been undoubtedly confirmed in our current reaction system and simultaneously, both $^{\bullet}O_2^-$ and $^{\bullet}OH$ radicals have contributed to the mineralization of RhB, a feasible photocatalytic mechanism in terms of interface-dipole-driven S-scheme charge flow model is proposed herein as shown in **Figure 6c**. In this unique organic-inorganic hybrid core-shell heterojunction, the polar amine groups along the polyelectrolyte PFN backbone function as donors and build an electron accumulated WO_3 surface and an electron depleted PFN surface in ground electronic state via directional interfacial charge transfer, thereby creating an interfacial dipole oriented from conjugated macromolecular backbone of PFN to the surface of WO_3 matrices. In this scenario, when the WO_3@PFN heterojunction is illuminated, the WO_3 and PFN assembly units are photoexcited to yield charge carriers; the presence of interface dipole activates the unidirectional S-scheme electron motion from the CB of WO_3 framework to the HOMO of the conjugated chain of PFN, ultimately leaving electrons and holes with substantial redox capacity in the LUMO level of PFN and VB level of WO_3, respectively. As a result, large numbers of $^{\bullet}O_2^-$, holes as well as $^{\bullet}OH$ are produced in the reaction system, leading to enhanced net efficiency of photoactivity within the WO_3@PFN heterojunction. Moreover, this distinctive interface engineering strategy can be extended to the construction of many other photocatalytic systems for accelerating the interfacial charge transfer (**Figure S23**). Thus, the methodology proposed in this work can be regarded as a general approach to the design of various efficient photosystems involving CPEs and also provide some illuminating insights into the study of the working mechanism of the CPEs interlayers in such devices.

3 Conclusions

In summary, we report a distinctive strategy to overcome the drawback of the weak interfacial driving source over heterojunction via polyelectrolyte-triggered interface dipole. This enabled synergistic modulation of the intrinsic driving force and band offsets at the interface and successfully led to significant boosts of the charge transfer kinetics of heterojunction. As revealed by our DFT simulations and experimental studies, the electronic coupling interaction between the pendant amine groups of PFN and the

semiconductor substrate (i.e., WO_3) was found to induce interfacial charge redistribution over WO_3@PFN heterostructure, thereby creating a directional microscopic electric dipole from PFN to WO_3. Consequently, the directional interface dipole can serve as a robust intrinsic driving force source for considerably accelerating the unidirectional S-scheme charge motion rate from WO_3 to PFN, endowing the WO_3@PFN core-shell heterojunction with significantly boosted photocatalytic performance. A detailed intrinsic mechanism in terms of interface dipole-driven charge flow was elucidated, and the role of the polar polyelectrolyte was clarified. The methodology proposed in this work would offer some insights for exploring advanced heterojunction photocatalysts for solar-to-chemical conversion and understanding the working mechanism of the polyelectrolyte interlayer.

Acknowledgments The authors are grateful to the financial support from the Guangdong International Science and Technology Cooperation Foundation (2020A0505100002), the 111 Project (BP0618009), the China Scholarship Council, Guangdong-Hong Kong-Macao Joint Laboratory of Optoelectronic and Magnetic Functional Materials (2019B121205002), the RGC Senior Research Fellowship Scheme (SRFS2021-5S01), the Hong Kong Research Grants Council (PolyU 15307321), Research Institute for Smart Energy (CDAQ) and Miss Clarea Au for the Endowed Professorship in Energy (847S). The authors would like to thank Miss Hanbo Yang from Imperial College London for wealthy discussion and helpful advice for the paper.

Conflict of interest The authors declare that they have no conflict of interest.

Supporting information The supporting information is available online at http://chem.scichina.com and http://link.springer.com/journal/11426. The supporting materials are published as submitted, without typesetting or editing. The responsibility for scientific accuracy and content remains entirely with the authors.

1 Lewis NS. *Science*, 2007, 315: 798-801
2 Hisatomi T, Kubota J, Domen K. *Chem Soc Rev*, 2014, 43: 7520-7535
3 Wang Z, Li C, Domen K. *Chem Soc Rev*, 2019, 48: 2109-2125
4 Wu X, Luo N, Xie S, Zhang H, Zhang Q, Wang F, Wang Y. *Chem Soc Rev*, 2020, 49: 6198-6223
5 Takata T, Jiang J, Sakata Y, Nakabayashi M, Shibata N, Nandal V, Seki K, Hisatomi T, Domen K. *Nature*, 2020, 581: 411-414
6 Albero J, Peng Y, García H. *ACS Catal*, 2020, 10: 5734-5749
7 Chen F, Ma T, Zhang T, Zhang Y, Huang H. *Adv Mater*, 2021, 33: 2005256
8 Nayak S, Swain G, Parida K. *ACS Appl Mater Interfaces*, 2019, 11: 20923-20942
9 Chen S, Qi Y, Hisatomi T, Ding Q, Asai T, Li Z, Ma SSK, Zhang F, Domen K, Li C. *Angew Chem Int Ed*, 2015, 54: 8498-8501
10 Zhang X, Meng Z, Rao D, Wang Y, Shi Q, Liu Y, Wu H, Deng K, Liu H, Lu R. *Energy Environ Sci*, 2016, 9: 841-849
11 Low J, Yu J, Jaroniec M, Wageh S, Al-Ghamdi AA. *Adv Mater*, 2017, 29: 1601694
12 Wang H, Zhang L, Chen Z, Hu J, Li S, Wang Z, Liu J, Wang X. *Chem Soc Rev*, 2014, 43: 5234-5244
13 Xu Q, Zhang L, Cheng B, Fan J, Yu J. *Chem*, 2020, 6: 1543-1559
14 Bao Y, Song S, Yao G, Jiang S. *Solar RRL*, 2021, 5: 2100118
15 Zhang L, Zhang J, Yu H, Yu J. *Adv Mater*, 2022, 34: 2107668
16 Wang L, Zhu B, Zhang J, Ghasemi JB, Mousavi M, Yu J. *Matter*, 2022, 5: 4187-4211
17 Fu J, Xu Q, Low J, Jiang C, Yu J. *Appl Catal B*, 2019, 243: 556-565
18 Cao S, Yu J, Wageh S, Al-Ghamdi AA, Mousavi M, Ghasemi JB, Xu F. *J Mater Chem A*, 2022, 10: 17174-17184
19 Ruan X, Huang C, Cheng H, Zhang Z, Cui Y, Li Z, Xie T, Ba K, Zhang H, Zhang L, Zhao X, Leng J, Jin S, Zhang W, Zheng W, Ravi SK, Jiang Z, Cui X, Yu J. *Adv Mater*, 2023, 35: 2209141
20 Li X, Kang B, Dong F, Zhang Z, Luo X, Han L, Huang J, Feng Z, Chen Z, Xu J, Peng B, Wang ZL. *Nano Energy*, 2021, 81: 105671
21 Wang L, Cheng B, Zhang L, Yu J. *Small*, 2021, 17: 2103447
22 Chen C, Hu J, Yang X, Yang T, Qu J, Guo C, Li CM. *ACS Appl Mater Interfaces*, 2021, 13: 20162-20173
23 Cheng C, Zhang J, Zhu B, Liang G, Zhang L, Yu J. *Angew Chem Int Ed*, 2023, 62: e202218688
24 He B, Wang Z, Xiao P, Chen T, Yu J, Zhang L. *Adv Mater*, 2022, 34: 2203225
25 Nguyen V-H, Singh P, Sudhaik A, Raizada P, Le QV, Helmy ET. *Mater Lett*, 2022, 313: 131781
26 Wu Y, Zhang X, Xing Y, Hu Z, Tang H, Luo W, Huang F, Cao Y. *ACS Materials Letters*, 2019, 1: 620-627
27 Hu Z, Zhang X, Yin Q, Liu X, Jiang X-f, Chen Z, Yang X, Huang F, Cao Y. *Nano Energy*, 2019, 60: 775-783
28 He Z, Wu H, Cao Y. *Adv Mater*, 2014, 26: 1006-1024
29 Tan Y, Chen L, Wu F, Huang B, Liao Z, Yu Z, Hu L, Zhou Y, Chen Y. *Macromolecules*, 2018, 51: 8197-8204
30 Huang F, Wu H, Cao Y. *Chem Soc Rev*, 2010, 39: 2500-2521
31 Bae S, Kim D, Kim H, Gu M, Ryu J, Kim B-S. *Adv Funct Mater*, 2020, 30: 1908492
32 Yeo J-S, Kang M, Jung Y-S, Kang R, Lee S-H, Heo Y-J, Jin S-H, Kim D-Y, Na S-I. *Nano Energy*, 2016, 21: 26-38
33 He Z, Zhong C, Su S, Xu M, Wu H, Cao Y. *Nat Photonics*, 2012, 6: 591-595
34 He Z, Zhong C, Huang X, Wong W-Y, Wu H, Chen L, Su S, Cao Y. *Adv Mater*, 2011, 23: 4636-4643
35 Feng C, Wang X, Chen G, Zhang B, He Z, Cao Y. *Langmuir*, 2021, 37: 4347-4354
36 Weng B, Wu J, Zhang N, Xu Y-J. *Langmuir*, 2014, 30: 5574-5584
37 Wang J, Chen Z, Zhai G, Men Y. *Appl Surf Sci*, 2018, 462: 760-771
38 Cao J, Luo B, Lin H, Xu B, Chen S. *Appl Catal B*, 2012, 111-112: 288-296
39 Hsieh H-C, Chen J-Y, Lee W-Y, Bera D, Chen W-C. *Macromol Rapid Commun*, 2018, 39: 1700616
40 Carulli F, Mróz W, Lassi E, Sandionigi C, Squeo B, Meazza L, Scavia G, Luzzati S, Pasini M, Giovanella U, Galeotti F. *Chemical Papers*, 2018, 72: 1753-1759
41 Lin X, Xu S, Wei Z-Q, Hou S, Mo Q-L, Fu X-Y, Xiao F-X. *J Mater Chem A*, 2020, 8: 20151-20161
42 Zhang Y, Fan X, Jian J, Yu D, Zhang Z, Dai L. *Energy Environ Sci*, 2017, 10: 2312-2317
43 Pan B, Xie Y, Zhang S, Lv L, Zhang W. *ACS Appl Mater Interfaces*, 2012, 4: 3938-3943
44 Maturová K, Kemerink M, Wienk MM, Charrier DSH, Janssen RAJ. *Adv Funct Mater*, 2009, 19: 1379-1386
45 Han T, Cao X, Sun K, Peng Q, Ye C, Huang A, Cheong W-C, Chen Z, Lin R, Zhao D, Tan X, Zhuang Z, Chen C, Wang D, Li Y. *Nat Commun*, 2021, 12: 4952
46 Kanata-Kito T, Matsunaga M, Takakura H, Hamakawa Y, Nishino T. *Proc. SPIE*, 1990, 1286: 56-65
47 Le Formal F, Sivula K, Grätzel M. *J Phys Chem C*, 2012, 116: 26707-26720
48 Feng C, Wang X, He Z, Cao Y. *Solar RRL*, 2021, 5: 2000753
49 Zhu M, Kim S, Mao L, Fujitsuka M, Zhang J, Wang X, Majima T. *J Am Chem Soc*, 2017, 139: 13234-13242
50 Song X-N, Wang C-Y, Wang W-K, Zhang X, Hou N-N, Yu H-Q. *Adv Mater Interfaces*, 2016, 3: 1500417
51 Han HS, Park W, Hwang SW, Kim H, Sim Y, Surendran S, Sim U, Cho IS. *J Catal*, 2020, 389: 328-336
52 Huang H, Tu S, Zeng C, Zhang T, Reshak AH, Zhang Y. *Angew Chem Int Ed*, 2017, 56: 11860-11864
53 Rao PM, Cai L, Liu C, Cho IS, Lee CH, Weisse JM, Yang P, Zheng X. *Nano Lett*, 2014, 14: 1099-1105
54 Baek JH, Kim BJ, Han GS, Hwang SW, Kim DR, Cho IS, Jung HS. *ACS Appl Mater Interfaces*, 2017, 9: 1479-1487
55 Bae S, De Guzman RAF, Jeon D, Kim M, Ryu J. *Adv Mater Interfaces*, 2023, 10: 2202101
56 Bae S, Kim H, Jeon D, Ryu J. *ACS Appl Mater Interfaces*, 2019, 11: 7990-7999
57 Zhu XY, Yang Q, Muntwiler M. *Acc Chem Res*, 2009, 42: 1779-1787